The temperature-dependent conformational ensemble of SARS-CoV-2 main protease (M^{pro})

Ali Ebrahim*[,1,2], Blake T. Riley*[,2], Desigan Kumaran[3], Babak Andi[4,5], Martin R. Fuchs[4], Sean McSweeney[4,5], Daniel A. Keedy[#,2,6,7]

1. Diamond Light Source, Harwell Science and Innovation Campus, Didcot OX11 0DE, England
2. Structural Biology Initiative, CUNY Advanced Science Research Center, New York, NY 10031
3. Biology Department, Brookhaven National Laboratory, Upton, NY 11973
4. National Synchrotron Light Source II, Brookhaven National Laboratory, Upton, NY 11973
5. National Virtual Biotechnology Laboratory (NVBL), US Department of Energy, Washington, DC, United States
6. Department of Chemistry and Biochemistry, City College of New York, New York, NY 10031
7. Ph.D. Programs in Biochemistry, Biology, and Chemistry, The Graduate Center – City University of New York, New York, NY 10016

* contributed equally
[#] correspondence to dkeedy@gc.cuny.edu

Abstract

The COVID-19 pandemic, instigated by the SARS-CoV-2 coronavirus, continues to plague the globe. The SARS-CoV-2 main protease, or M^{pro}, is a promising target for development of novel antiviral therapeutics. Previous X-ray crystal structures of M^{pro} were obtained at cryogenic temperature or room temperature only. Here we report a series of high-resolution crystal structures of unliganded M^{pro} across multiple temperatures from cryogenic to physiological, and another at high humidity. We interrogate these datasets with parsimonious multiconformer models, multi-copy ensemble models, and isomorphous difference density maps. Our analysis reveals a temperature-dependent conformational landscape for M^{pro}, including a mobile water interleaved between the catalytic dyad, mercurial conformational heterogeneity in a key substrate-binding loop, and a far-reaching intramolecular network bridging the active site and dimer interface. Our results may inspire new strategies for antiviral drug development to counter-punch COVID-19 and combat future coronavirus pandemics.

Introduction

COVID-19 is a global pandemic disease caused by severe acute respiratory syndrome coronavirus 2. SARS-CoV-2 is a highly infectious, airborne, respiratory virus, which has caused over 100 million infections and 2 million deaths worldwide as of February 2021. In the past year, several approaches to prevent and treat COVID-19 have been successfully developed, including new vaccines, monoclonal antibody treatments [1], and repurposed existing therapeutics [2,3]. However, development of novel small-molecule antiviral drugs has lagged behind. New antiviral drugs would not only provide a powerful weapon against COVID-19 for infected patients and frontline workers, but would also aid in preparation for future coronavirus pandemics.

A promising target for potential new antiviral drugs against SARS-CoV-2 is a chymotrypsin-like protease known by several names: non-structural protein 5, nsp5, 3C-like protease, $3CL^{pro}$, main protease, or M^{pro}. M^{pro} is part of a polyprotein encoded by the viral RNA genome. After being excised from the polyprotein by its own proteolytic activity, M^{pro} cleaves at no fewer than 11 sites in the polyprotein to generate individual functional proteins [4] that help the virus replicate. Due to its importance to the SARS-CoV-2 life cycle, M^{pro} has been identified as a key target for COVID-19 drug design.

Drug design efforts focused on M^{pro} have been aided by insights from structural biology. The first SARS-CoV-2 M^{pro} crystal structures were released in the Protein Data Bank (PDB) [5] early in the pandemic, within the first week of February 2020 [6]. These structures revealed that, like SARS-CoV M^{pro} before it, SARS-CoV-2 M^{pro} is composed of two β-barrel domains known as domain I and domain II, and an α-helical bundle known as domain III (**Fig. 1a**). The active site cavity is located on the surface, with the His41–Cys145 catalytic dyad positioned between domain I and domain II. Domain III

is involved in regulating dimerization [7], which is critical for coronavirus M^{pro} catalytic activity [8,9]. Since the initial structures of SARS-CoV-2 M^{pro}, X-ray crystallography has been used to identify promising ligand binding sites and alternative structural states of the protein, resulting in a total of over 250 available structures. These efforts included co-crystallography with an eye toward drug repurposing [10,11], as well as crystallographic screens of non-covalent and covalent small-molecule fragments to establish new toe-holds for *ab initio* drug design [12] which were then leveraged via a crowd-sourced process to design novel inhibitors [13].

As with much modern protein crystallography, the above experiments were performed at cryogenic temperatures, which can bias protein conformational ensembles [14,15]. To bypass this limitation, a room-temperature crystal structure of unliganded M^{pro} was reported [16] (PDB ID 6WQF). Although its resolution was only moderate (2.3 Å), it nevertheless revealed evidence of conformational plasticity near the active site that was distinct relative to past cryogenic structures. Subsequent work built on this foundation of room-temperature crystallography to dissect M^{pro} function [17,18]. However, no studies to date have reported crystal structures of M^{pro} across a wide range of temperatures. Previously, such a multitemperature crystallography strategy was instrumental for revealing novel aspects of correlated active-site conformational heterogeneity in a dynamic proline isomerase [19] and of long-range allosteric signaling in a therapeutic-target tyrosine phosphatase [20].

Here we report high-resolution crystal structures of SARS-CoV-2 M^{pro} at five temperatures: 100 K (cryogenic), 240 K (above the so-called glass transition or dynamical transition [19]), 277 K ("room temperature" in many crystallography studies), 298 K (ambient), and 310 K (physiological). We also report a structure at ambient temperature but high relative humidity (99.5% RH) to gauge the relative effects of temperature vs. humidity on M^{pro}. To our knowledge, this study represents the first experimentally based structural analysis for any SARS-CoV-2 protein at variable temperature and/or humidity. For all datasets we have constructed parsimonious multiconformer models as well as

multi-copy crystallographic ensemble models, which provide complementary insights into protein structural flexibility as a function of temperature. Together, our data reveal a network of subtle but provocative temperature-dependent conformational heterogeneity, not only at the catalytic site but also spanning several functionally relevant sites throughout M^{pro}, which may help motivate an allosteric strategy for antiviral drug design to combat COVID-19 and/or future coronavirus pandemics.

Results

Multitemperature crystallographic data collection and modeling

Data were obtained from single M^{pro} crystals using helical data collection, to maximize diffraction intensity while minimizing radiation damage (**Supp. Fig. 1**). To probe the conformational landscape of M^{pro}, we obtained high-resolution structures at five different temperatures: 100 K, 240 K, 277 K, 298 K (ambient; see Methods), and 310 K. Our datasets thus span a broad temperature range: cryogenic, just above the glass transition or dynamic transition [19], the range often noted as room temperature (roughly 293–300 K), and approximately physiological temperature. We also collected another 298 K dataset with high relative humidity (99.5% RH).

For all but the 277 K dataset (2.19 Å), the resolution was 2 Å or better (**Table 1**). The highest resolution was for the 100 K dataset (1.55 Å). Even at the higher temperatures, we saw little to no evidence of radiation damage (**Supp. Fig. 1**). After data reduction, we created a multiconformer model for each temperature, which includes a single conformer for most portions of the structure but alternative conformations where appropriate [21]. See Methods for more details on data collection and modeling, and **Table 1** for overall diffraction data and refinement statistics.

Structure	100 K	240 K	277 K	298 K	298 K, 99.5% RH	310 K
PDB ID	7MHF	7MHG	7MHH	7MHI	7MHJ	7MHK
Resolution (Å)	48.07–1.55	55.62–1.53	48.96–2.19	56.29–1.88	56.30–2.00	43.97–1.96
Completeness (%)	99.7 (96.0)	100 (99.4)	99.9 (98.7)	100 (100)	99.0 (97.4)	99.9 (100)
Multiplicity	3.4 (3.4)	6.6 (6.2)	6.9 (6.9)	6.8 (6.9)	6.8 (6.7)	6.6 (6.7)
I/sigma(I)	3.3 (1.0)	7.9 (0.9)	4.5 (1.1)	5.0 (0.4)	6.3 (0.6)	5.4 (0.3)
R_{merge}(I)	0.158 (0.507)	0.180 (1.463)	0.292 (1.805)	0.182 (2.353)	0.178 (1.708)	0.195 (1.805)
R_{meas}(I)	0.188 (0.604)	1.960 (1.600)	0.316 (1.954)	0.197 (2.548)	0.193 (1.854)	0.213 (1.957)
R_{pim}(I)	0.100 (0.325)	0.076 (0.639)	0.119 (0.742)	0.076 (0.967)	0.074 (0.711)	0.084 (1.046)
$CC_{1/2}$	0.977 (0.695)	0.995 (0.356)	0.985 (0.799)	0.990 (0.285)	0.989 (0.376)	0.990 (0.352)
Wilson B-factor	16.164	16.370	31.769	29.670	34.350	33.810
Total observations	127548	263470	97820	152368	125878	128140
Unique observations	37901	39975	14120	22459	18588	19444
Space group	C121	C121	C121	C121	C121	C121
Unit cell dimensions (Å,Å,Å,°,°,°)	113.71, 53.32, 44.57, 90, 102.96, 90	114.19, 53.49, 45.00, 90, 103.04, 90	115.02, 54.36, 44.97, 90, 101.50, 90	114.74, 54.57, 45.11, 90, 101.65, 90	114.88, 54.74, 45.24, 90, 101.42, 90	114.3, 54.29, 44.97, 90, 102.12, 90
Solvent content (%)	35.88	36.40	38.95	39.53	39.89	38.36
R_{work}	0.1834	0.1701	0.1994	0.1847	0.1942	0.2039
R_{free}	0.2223	0.2043	0.2547	0.2276	0.2421	0.2482
RMS bonds (Å)	0.006	0.011	0.002	0.003	0.004	0.003
RMS angles (°)	0.888	1.094	0.472	0.569	0.702	0.576
Ramachandran outliers (%)	0.33	0.33	0.33	0.00	0.33	0.66

Ramachandran favoured (%)	97.70	98.36	96.71	97.37	96.38	97.37
Clashscore	3.81	2.42	2.31	1.89	2.31	2.73
MolProbity score	1.24	1.02	1.22	1.07	1.25	1.18

Table 1: Crystallographic statistics for multitemperature datasets and multiconformer models. Overall statistics given first (statistics for highest-resolution bin in parentheses). RH = relative humidity. RMS = root-mean-square deviation from ideal values. For Phenix ensemble model refinement statistics, see **Table 2**.

Overall structure as a function of temperature

The global structure of M^{pro} in our crystals remains similar across temperatures (**Fig. 1d, Supp. Fig. 2**), as expected. Indeed, the maximum Cα RMSD between any pair of structures in the ambient-humidity multitemperature series is only 0.64 Å, and the maximum all-atom RMSD is only 0.98 Å. However, there is a clear clustering between lower-temperature (240, 277 K) and higher-temperature (277, 298, 310 K) structures, based on either Cα RMSD (**Fig. 1d**) or all-atom RMSD (**Supp. Fig. 2**). These observations indicate that aspects of the M^{pro} conformational landscape change in response to temperature.

Humidity also appears to have some effect on M^{pro} structure, as evidenced by the fact that the overall largest pairwise Cα RMSD (0.65 Å, **Fig. 1d**) and all-atom RMSD (1.04 Å, **Supp. Fig. 2**) involve the 298 K high-humidity (99.5% RH) structure. However, the corresponding RMSD values for the 298 K ambient-humidity (36.7% RH) structure are only slightly smaller (<0.1 Å difference). These RMSD differences between high vs. low humidity are minor compared to the differences between the high vs. low temperature clusters mentioned above. Thus, temperature affects M^{pro} structure noticeably more than does humidity. This result contrasts with previous studies of lysozyme in which similar protein structural alterations were achieved by either small changes in humidity or large changes in temperature [22]; this discrepancy may result from different protein:solvent arrangements in the lysozyme vs. M^{pro} crystal lattices.

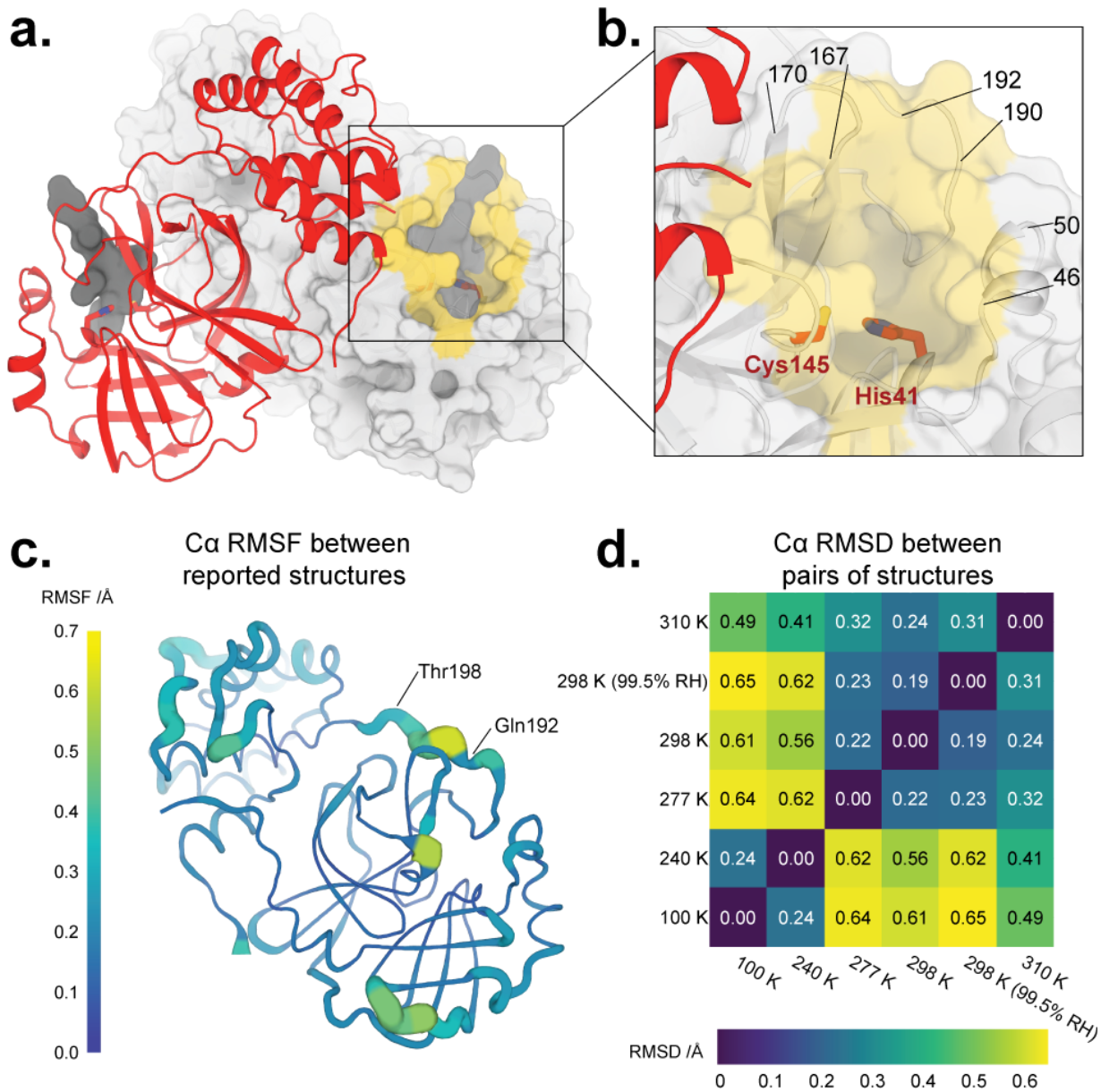

Figure 1: Overall structure of SARS-CoV-2 main protease at multiple temperatures.
a. New X-ray crystal structure of apo M^{pro} at physiological temperature (310 K) (red). The biological dimer involving the other monomer (light grey surface) is constituted via crystal symmetry. The competitive inhibitor N3 from a previous structure (PDB ID: 6LU7) (semi-transparent, dark grey surface) is shown in both protomers for context.
b. Close-up view of the M^{pro} active site region, including the catalytic dyad of Cys145 and His41 (red sticks) and highlighting residues that form the substrate binding pocket (yellow surface).
c. Cartoon putty representation of conformational variability between new M^{pro} structures described in this work: 100 K, 240 K, 277 K, 298 K, 298 K (99.5% RH), and 310 K. Thickness and color indicate root-mean-square fluctuations (RMSF) of Cα atom positions, from low (thin, dark blue) to high (thick, yellow). The largest differences between these structures' backbones occur between residues 192–198. Same view as **a.** See also **Supp. Fig. 3**.
d. Heatmap of pairwise Cα atom root-mean-square deviation (RMSD) between final refined structures, revealing temperature-dependent clustering (top-right vs. bottom-left). See also **Supp. Fig. 2**.

Temperature dependence of local alternative conformations

To provide more detailed insights into the observed global temperature dependence, we sought to identify alternative conformations at the local scale that were stabilized or modulated by the temperature shifts in our experiments. We specifically focused our attention on areas of the protein that are of interest for drug design and/or biological function: the active site, nearby loops associated with substrate binding, and the dimer interface.

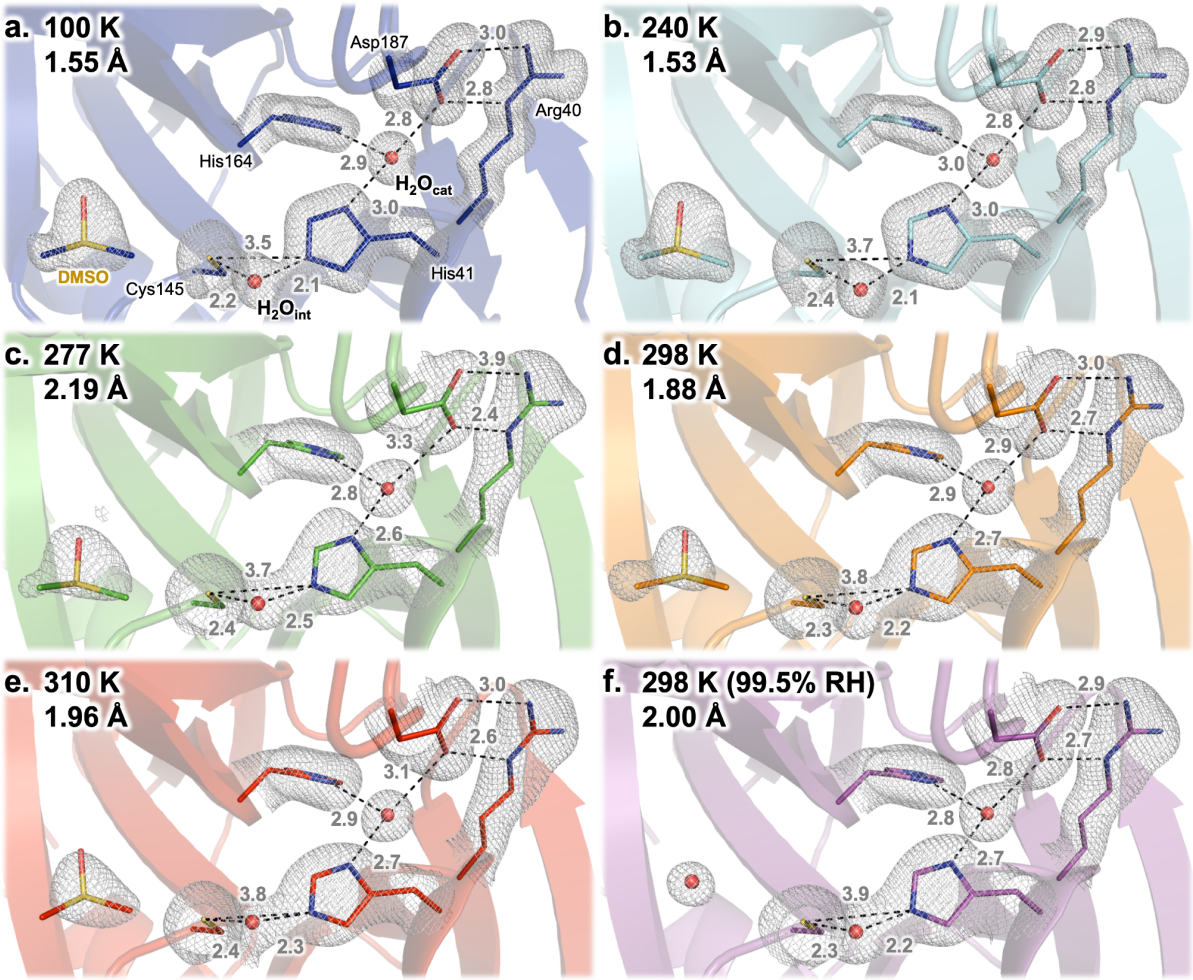

Figure 2: The unliganded M^{pro} active site as a function of temperature and humidity.
$2F_o$-F_c electron density (1.0 σ, gray mesh) and interatomic distances (pink, in Å) shows that the active-site structure remains similar across datasets, including the catalytic dyad of His41 and Cys145 and the presumed catalytic water (H_2O_{cat}). One minor exception is a different water, H_2O_{int}, which tends to shift upward in this view as temperature increases, adjusting its interactions with His41 and Cys145 (see also **Fig. 3**). An ordered DMSO molecule from the crystallization solution is visible at the left of each panel, except for 298 K at high humidity (99.5% RH) in which case a water is present at the same site instead.

First, the M^{pro} active site structure remains mostly consistent across our temperature series (**Fig. 2**). The catalytic amino acids are in very similar conformations across temperatures. Additionally, a key active-site water molecule (known as H_2O_{cat}), which hydrogen-bonds to both of the side chains of the catalytic dyad (His41 and Asp187), remains in the same position across our structures (**Fig. 2**). It has been suggested [16] that this water may play the role of a third catalytic residue (in addition to the catalytic dyad of His41 and Cys145). As previously noted [16], H_2O_{cat} is not modeled in some cryogenic structures — but it is modeled in 56% (142/252) of the publicly available structures of SARS-CoV-2 M^{pro} as of Feb. 4, 2021 (the vast majority of which are cryogenic), and perhaps should have been modeled in others [23].

As with the active-site amino acids and H_2O_{cat}, a dimethyl sulfoxide (DMSO) molecule from the crystallization solution is ordered nearby in each structure in the multitemperature series (**Fig. 2**, left of each panel). Interestingly, however, this DMSO is displaced by a water molecule in the high-humidity dataset (298 K, 99.5% RH), suggesting that the solvation distribution of the M^{pro} active site is malleable.

Another active-site water, which we refer to as the “intervening water” or H_2O_{int}, is also present in each of our structures. However, unlike H_2O_{cat}, H_2O_{int} is modeled in only <1% (2/252) of available structures: 7K3T (high-resolution apo; B.A., D.K., M.R.F., S.M. *et al., in preparation*) and 7JFQ (“de-oxidized C145”, no publication). There are experimental differences among the structures that do have H_2O_{int} modeled — for example, 7JFQ is in a different space group with different crystallization conditions — so it is not immediately obvious what causes this water to sometimes be visibly ordered. Interestingly, in our temperature series, H_2O_{int} is not static, but rather varies in position across temperatures by nearly 1 Å (**Fig. 3a**), which is significantly in excess of the estimated coordinate error of 0.18–0.34 Å for our structures. Together with its absence in many other structures, this suggests that H_2O_{int} is in

some sense mobile. There is a rough trend of higher temperatures corresponding to H_2O_{int} positions farther from the backbone of His41 and Cys145 and closer to His164, although this is not a strict rule. At 298 K, H_2O_{int} is in an almost identical position regardless of humidity (ambient or 99.5% RH), suggesting both that environmental humidity has minimal effects on these crystals and again that our structural results with respect to temperature dependence may be precise. Some positional uncertainty may stem from the fact that the $2F_o$-F_c electron density for this water is not fully discrete, but rather appears contiguous with the density for the adjacent catalytic His41 and Cys145 side chains (at typical map σ levels; **Fig. 2**).

Although H_2O_{int} is absent from the vast majority of the other hundreds of crystal structures of M^{pro}, it is displaced or "mimicked" by ligands in some instances. For example, a Zn^{2+} ion from an ionophore binds in the same position in 7B83 [11] (**Fig. 3b**). Interestingly, zinc was shown to bind to other viral M^{pro} enzymes, and to exhibit antiviral effects against several coronaviruses and non-coronaviruses, although the mechanism was thought to be via a different protein target [11]. In another example, H_2O_{int} is seemingly displaced by a carbonyl group in the linker of several covalent ligands that target the catalytic Cys145 in two dozen PDB structures from various groups associated with various published and unpublished studies (**Fig. 3c**). Interestingly the swath of positions for this carbonyl oxygen, including a more extreme position due to a distinct conformation of the linker (PDB 6XFN), seems to align with the swath of H_2O_{int} positions across our temperature series (plus 7K3T and 7JFQ) (**Fig. 3c**). Together, these data suggest a structural niche for H_2O_{int} that, regardless of its potential role in the catalytic mechanism, may be productively exploited for small-molecule ligand design.

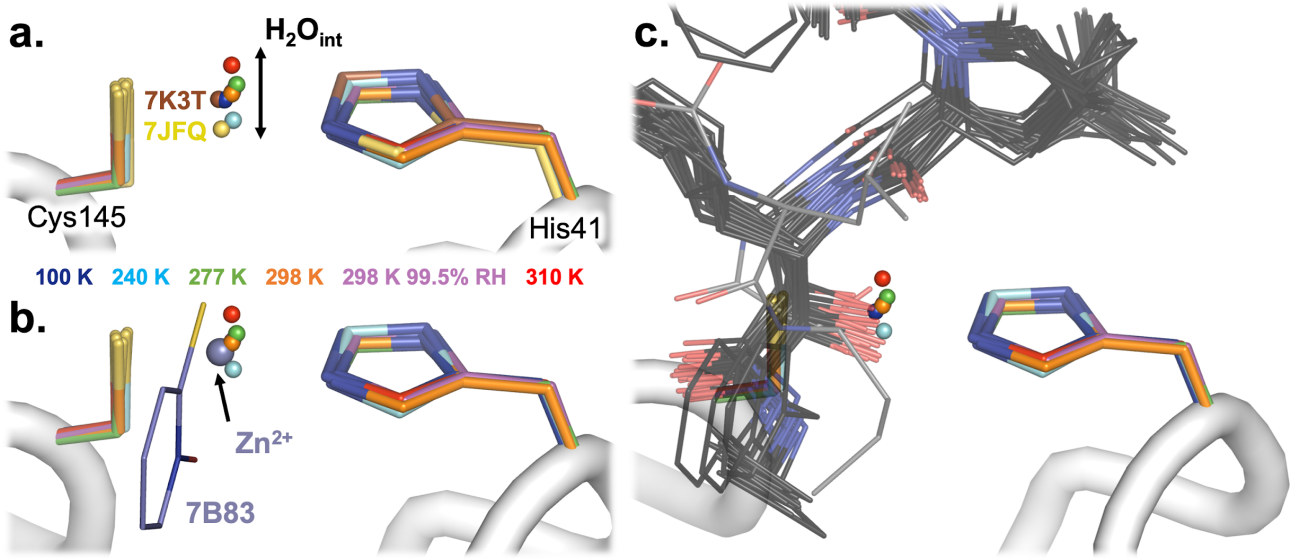

Figure 3: The rare active-site intervening water (H_2O_{int}) is sensitive to temperature and mimicked by ligands.

a. In our new structures, H_2O_{int} is ordered between Cys145 and His41 of the M^{pro} catalytic dyad, but its position varies as a function of temperature (blue to red). 298* K = 298 K at 99.5% relative humidity. The position of H_2O_{int} in the 298 K model collected at 99.5% relative humidity occupies an extremely similar position as that of H_2O_{int} in the 298 K model (orange). In only 2/252 previous structures of SARS-CoV-2 M^{pro} (7K3T and 7JFQ, both 100 K) is H_2O_{int} also ordered.

b-c. H_2O_{int} is mimicked/displaced by particular atoms in other previous structures of M^{pro}. Together these encompass the swath of H_2O_{int} positions.

b. In 7B83, Zn^{2+} from zinc pyrithione (purple) displaces H_2O_{int}.

c. In several structures from different series of covalent ligands (grey) linked to Cys145, a carbonyl oxygen of the covalent linker displaces H_2O_{int}. One of these linkers has a distinct conformation (6XFN, lighter grey), which places the carbonyl oxygen at a more extreme position corresponding to H_2O_{int} in our 310 K structure. Together these binders approximate the swath of H_2O_{int} positions in our multitemperature series.

Beyond the active site, we turned our attention to the nearby P5 binding pocket, specifically the loop composed of residues 192–198. Previously, the first report of a room-temperature structure of M^{pro}, which was in the apo form (PDB ID: 6WQF) [16], noted that this loop adopted a different conformation than in a prior 100 K apo structure (PDB ID: 6Y2E) [7], including rotated peptide orientations for Ala194–Gly195 and Asp197–Thr198. However, all of the structures in our multitemperature series, including at lower temperatures (100 K and 240 K), have a single backbone conformation in this region that matches that of 6WQF (**Fig. 4a**). In addition, other apo cryogenic structures, including one at high (1.2 Å) resolution (PDB ID: 7K3T), also match the 6WQF backbone conformation. All of these structures (6WQF, 6Y2E, 7K3T, and our multitemperature series) derive from the same crystal form

(**Table 1**). Thus, it appears the different loop conformation adopted in 6Y2E is not driven by temperature [16], nor by ligand binding or crystal lattice effects, but rather by some other aspect of the crystallization details or sample handling conditions — including, perhaps, idiosyncratic effects of crystal cryocooling [15,24]. Our conclusion here is also supported by a recent retrospective analysis of existing structures [23].

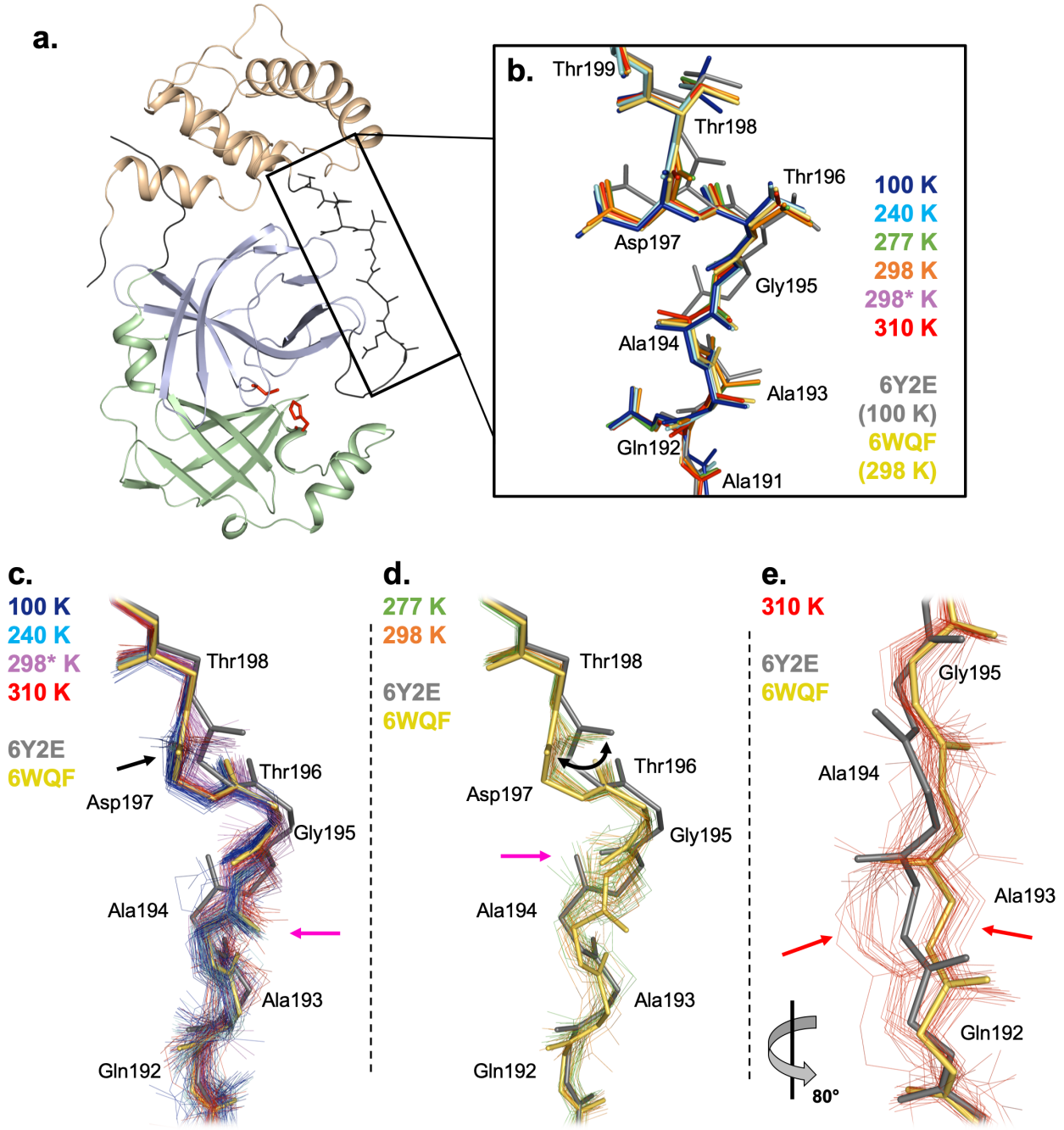

Figure 4: Complex temperature dependence of residues 192–198 in the P5 binding pocket.
a. M^{pro} monomer from cryogenic structure, coloured by domain: domain I, residues 8–101, pale green; domain II, residues 102–184, pale blue; domain III, residues 201–303, pale orange. Catalytic dyad residues Cys145 and His41 are shown as sticks (red). Terminal residues are shown in dark grey. P5 binding pocket linker loop (residues 190–200) shown in dark grey and as sticks (black box).
b. Our new multitemperature structures all have a single backbone conformation for this linker loop region. Regardless of temperature, they all match a similar backbone conformation to the room-temperature 6WQF model (yellow), and not the cryogenic 6Y2E model (grey) [16]. (298* K = 298 K, 99.5% relative humidity.)
c-e. Phenix ensemble refinement models based on our multitemperature datasets reveal a complex pattern of flexibility that was "hidden" in **b.**
c. For some conditions (100 K, blue; 240 K, cyan; 310 K, red; 298* K, magenta), the ensemble models generally match 6WQF, albeit with variability around the average conformation. For the Ala194–Gly195 peptide (pink arrow), all four conditions match 6WQF. For the Asp197–Thr198 peptide (black arrow), 100 K, 240 K, and 310 K match 6WQF, whereas 298* K adopts a swath of orientations at the Asp197–Thr198 peptide, bridging 6WQF and 6Y2E.
d. For other conditions (277 K, green; 298 K, orange), the ensemble models exhibit shifts away from 6WQF and toward 6Y2E. For the Ala194–Gly195 peptide, both conditions match 6Y2E (pink arrow) instead of 6WQF. For the Asp197–Thr198 peptide, both conditions adopt a swath of orientations (black curved arrow) bridging 6WQF and 6Y2E, similarly to 298* K (in **c**).
e. A zoomed-in and ~80° rotated view of the 310 K ensemble model illustrates a split between the primary conformation and a distinct alternative conformation, centered on Ala193 (red arrows). This split is unique to the 310 K ensemble model.

Crystallographic ensemble models reveal distinct backbone conformational heterogeneity

We next aimed to complement this analysis of our manually built multiconformer models with a more automated and explicitly unbiased approach to modeling flexibility that can handle larger-scale backbone flexibility such as loop motions. Therefore, we turned to Phenix ensemble refinement, which uses molecular dynamics simulations with time-averaged restraints to crystallographic data [25]. Phenix ensemble models have been used fruitfully for many applications [26], including exploring the effects of temperature on protein crystals [15], assessing the conformational plasticity of peptide–MHC interactions [27], and rational protein design [28]. After a scan of parameter space (see Methods), we created one ensemble model per temperature, each of which contains 18 to 45 constituent models (**Table 2**). Compared to the multiconformer models, the ensemble models fit the experimental data equally well or better based on R_{free}, albeit with slightly wider R_{free}-R_{work} gaps (**Table 2** vs. **Table 1**).

Structure	100 K	240 K	277 K	298 K	298 K, 99.5% RH	310 K
PDB ID	7MHL	7MHM	7MHN	7MHO	7MHP	7MHQ
Resolution (Å)	1.55	1.53	2.19	1.88	2.00	1.96
p_{TLS}	1	1	1	1	1	1
$w_{x\text{-}ray}$	2.5	2.5	2.5	2.5	2.5	2.5
# models in ensemble	45	43	18	20	36	42
R_{work}	0.1700	0.1606	0.1626	0.1667	0.1592	0.1686
R_{free}	0.2235	0.1978	0.2169	0.2077	0.2174	0.2240

Table 2: Refinement statistics for Phenix ensemble models. p_{TLS} and $w_{x\text{-}ray}$ are input parameters to Phenix ensemble refinement; the other input parameter (τ_x) was automatically determined (see Methods).

Using these ensemble models, we reexamined the P5 binding pocket loop mentioned above. The 100, 240, and 310 K ensemble models are similar to the previous “room-temperature” structure 6WQF, with mostly the same peptide orientation for Ala194–Gly195 and Asp197–Thr198 (**Fig. 4c**). By contrast, the 277 and 298 K ensemble models match the flipped Ala194–Gly195 peptide orientation from the previous cryogenic structure 6Y2E, and sample a swath of conformations for Asp197–Thr198 that span 6WQF and 6Y2E (**Fig. 4d**). Interestingly, although the 298 K 99.5% RH model follows a similar Ala194–Gly195 peptide orientation to 100, 240 and 310 K, it also exhibits a swath of peptide conformations for Asp197–Thr198, similar to our 277 and 298 K ensemble models. The distinction between ensembles that match 6WQF vs. 6Y2E is not simply a byproduct of resolution: although 277 K has the lowest resolution (2.19 Å), 298 K (1.88 Å) has a better resolution than 310 K (1.96 Å). Further, our 310 K ensemble reveals a distinct conformational split in this loop region, centered on Ala193, indicated by a subset of models within the ensemble following the primary conformation and a second subset following a separate, different conformation (**Fig. 4e**). Taken together, these results suggest that this region may have complex temperature dependence, as well as the capacity to sample alternative conformations that are “captured” in particular individual structures.

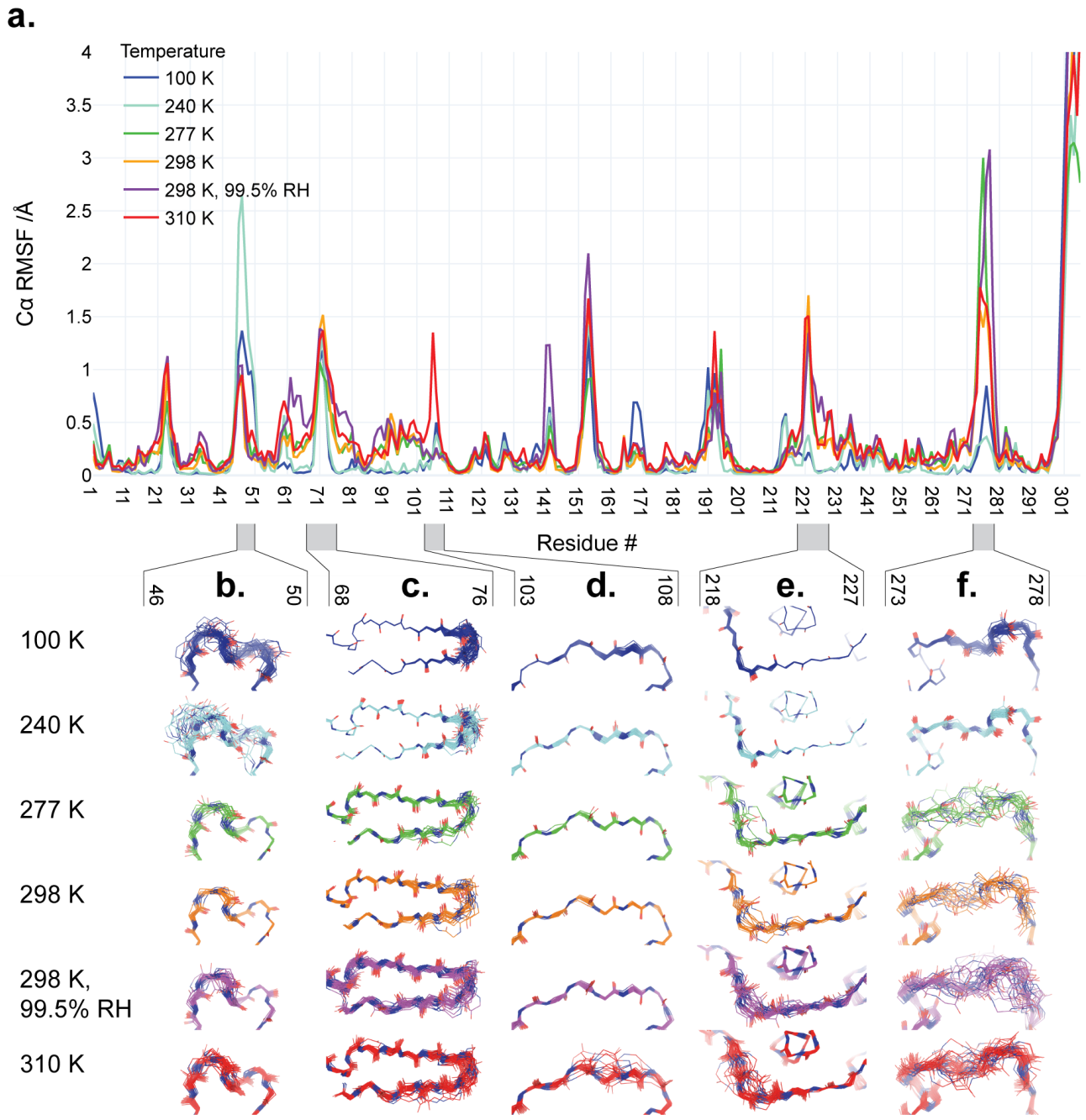

Figure 5: Backbone structural variability of ensemble models along the M^{pro} sequence as a function of temperature.

a. Root-mean-square fluctuation (RMSF) of Cα backbone atom positions is plotted vs. residue number for each of the different structures in our multitemperature series (colors in legend). RMSF spikes at the N-terminus, C-terminus, and β-turn 153–157 (in contact with the C-terminus) in the ensemble models are truncated in this plot, and should be interpreted with caution.

b-f. Backbone structures from ensemble refinement are shown for regions coinciding with temperature-dependent RMSF peaks. The refined single structure is shown as a cartoon, while atoms in the backbone of ensemble models are shown as lines.

Beyond just the P5 loop, we also examined other regions with elevated and/or temperature-dependent ensemble Cα root-mean-square fluctuation (RMSF) (**Fig. 5a**) that were not previously noted as being temperature-dependent. These regions segregate into different categories with distinct temperature dependence.

First, some regions display a generally positive correlation between backbone structural variability and diffraction experiment temperature. For example, residues 218–227 (**Fig. 5e**) and 273–278 (**Fig. 5f**) are highly ordered at 100 K and 240 K, but mobile at warmer temperatures. These regions are spatially contiguous in the monomer, within the helical domain III. In another case, residues 68–76 (**Fig. 5c**), conformational diversity is restricted to the β-hairpin at 100 K and 240 K, but appears to spread further down the β-strands at higher temperatures. Interestingly, although 68–76 is isolated from the regions described earlier (218–227 & 273–278) in the monomer and the biologically-relevant dimer, it is contiguous with them in the crystal lattice. In contrast to these regions with quasi-continuous temperature dependence, we observe a more abrupt response for residues 103–108 (**Fig. 5d**), which shows significant backbone heterogeneity only at 310 K. Notably, this region is spatially separated (within the monomer, dimer, and lattice) from the regions mentioned above that have a less abrupt temperature response. Finally, we observe one region with a negative correlation between backbone variability and temperature: the short 3_{10} helix at residues 46–51 (**Fig. 5b**). This region abuts the P5 substrate binding loop composed of residues 192–198 with its complex temperature dependence (**Fig. 4**); together, these two regions form one side of the active site pocket (**Fig. 1b**).

A network of coupled conformational heterogeneity bridges the active site, substrate pocket, inter-domain interface, and dimer interface

To complement the model-centric approaches above, we also looked for temperature-dependent conformational effects using an approach that is more directly data-driven: isomorphous F_o-F_o difference electron density maps. We computed F_o-F_o difference maps for each temperature vs. 100 K, and looked for patterns in terms of spatial colocalization of difference peaks. The global results confirm that the protein structure remains similar overall, with a smattering of difference peaks throughout the monomer asymmetric unit (**Supp. Fig. 4**). However, within those difference peaks lies a provocative stretch of difference features spanning the dimer interface, the interface between domain I and domain II of the monomer, and the edge of the P5 substrate binding pocket (**Fig. 6**). These difference features may be somewhat resolution-dependent, as they are least pronounced for 277 K (2.19 Å) and most pronounced for 240 K (1.53 Å), but their distribution across M^{pro} is qualitatively similar across temperatures.

A closer examination of the models in the vicinity of these difference features reveals what appears to be a series of correlated conformational motions keyed to temperature change. For example, F_o-F_o density shows that Glu290 shifts from a single side-chain rotamer at 100 K to two alternative rotamers with partial occupancies at 240 K (**Fig. 6a**); this second rotamer seen at 240 K then remains as a single full-occupancy conformation for all higher temperatures. In sync with Glu290, our multiconformer models show that the adjacent Cys128 shifts its conformational distribution, but in the opposite fashion: from two alternative rotamers to one (**Fig. 6a**). Both Glu290 and Cys128 interact with a symmetry-related Arg4 across the biological dimer interface (**Fig. 6b**). Interestingly, two small-molecule fragments from recent crystallographic screens [12,29] bind at this area of the dimer interface (**Fig. 6a-b**). Moreover, ordered polyethylene glycol (PEG) molecules from several previous

structures illustrate the potential for future ligand design efforts to “grow” from one of these initial fragment hits (5RF0) toward the mobile Glu290 and Cys128. This observation reinforces the idea that molecules from crystallization solutions, such as glycols, can reveal useful features like cryptic binding pockets [30].

Glu290 is connected to another interesting residue, Asp197, via a hydrogen-bond network with only one intervening side chain (Arg131). Asp197 becomes more ordered at higher temperature based on increasingly positive F_o-F_o density, while an interacting water molecule is simultaneously liberated (**Fig. 6c**) and an adjacent residue, Thr198, shifts from two alternative side-chain rotamers to just one. The Thr198 motion is linked to a conformational change for the nearby Glu240 side chain and Pro241 backbone, thus establishing a possible means for allosteric communication across the inter-domain interface. In the opposite direction from Asp197, other adjacent residues experience changes in ordering per F_o-F_o peaks; these residues together form the 192–198 loop of the functionally important and mobile P5 pocket (**Fig. 4**) leading toward the active site.

Overall, these observations describe a series of conformational motions that bridge the dimer interface, inter-domain interface, substrate binding pocket, and active site (**Fig. 6** *center*, boxes and oval). In this work, temperature is the perturbation/effector — but our results raise the enticing possibility that future small molecules could be used to allosterically perturb this network, thereby modulating enzyme dimerization and/or catalysis.

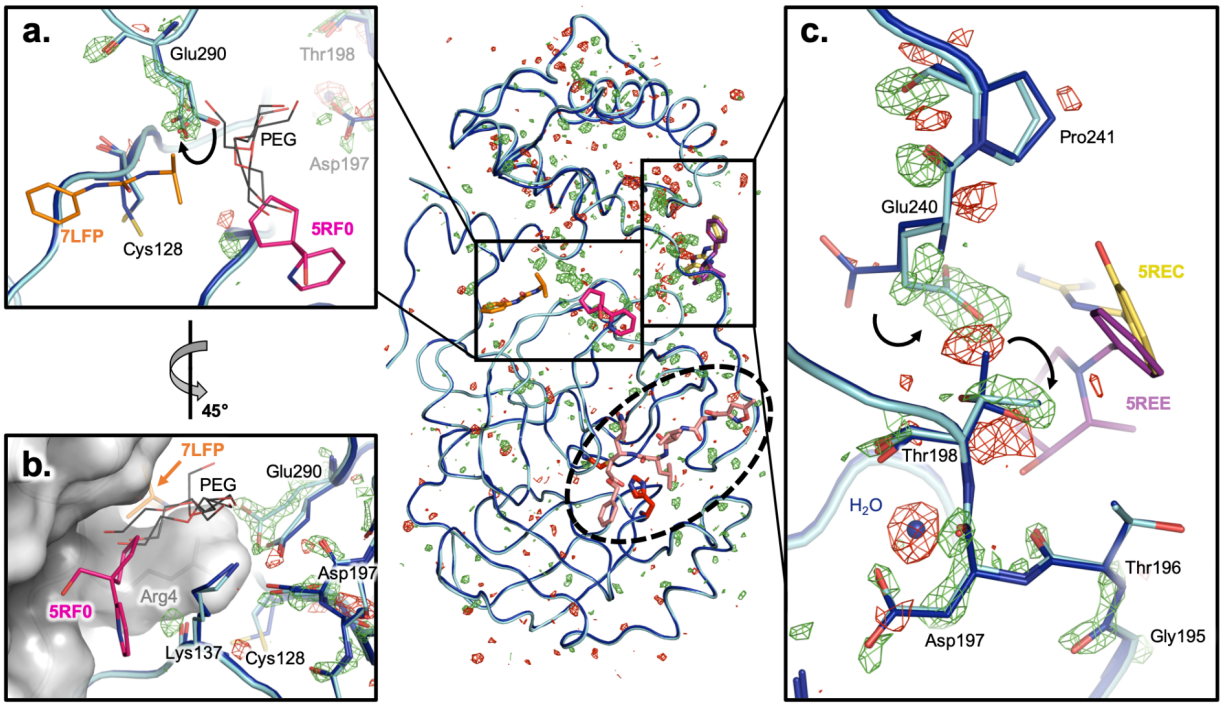

Figure 6: F_o-F_o difference maps reveal local conformational shifts connecting the active site, inter-domain interface, and dimer interface.
Center: Overview of isomorphous F_o-F_o difference electron density map at +/-3 σ (green/red mesh) for the 240 K dataset (cyan) minus the 100 K dataset (dark blue). (See **Supp. Fig. 4** for F_o-F_o maps for all temperatures). Ligands from cocrystal structures are shown at the active site (dashed oval) (pale orange, 6LU7), inter-domain interface (purple, 5REE; yellow, 5REC), and dimer interface (orange, 7LFP; pink, 5FR0).
a. Glu290 switches from one side-chain rotamer at 100 K to two alternative rotamers at 240 K (curved arrow). Glu290 is spatially adjacent to Cys128, which switches from two alternative rotamers at 100 K to a single rotamer at 240 K in our multiconformer models. These residues are near two ligands from separate crystallographic screens (7LFP, 5RF0), as well as many ordered PEG molecules from the crystallization cocktails of various structures (7KVR, 7KVL, 7KFI, 7LFE).
b. A ~45° rotated view relative to **a.** shows that these two ligands bind at the dimer interface of the biological monomer, constituted in the crystal from a symmetry-related protomer (grey surface). This interface also includes the Asp197 region (right).
c. Asp197 becomes more ordered at 240 K, while an interacting water molecule (blue sphere) becomes less ordered or displaced. Meanwhile, Thr198 switches from two alternative side-chain rotamers at 100 K to a single rotamer at 240 K, which causes Glu240 — located across the inter-domain interface — to change side-chain rotamer (curved arrows), with additional effects on the adjacent backbone of Pro241. In the other direction from Asp197 (down in this view), other residues in the P5 substrate binding pocket loop (**Fig. 4**) undergo conformational adjustments en route to the active site.

Discussion

Our crystal structures of unliganded SARS-CoV-2 M^{pro} at variable temperature and humidity paint a picture of a complex protein conformational landscape. The structure of M^{pro} does not change linearly with temperature; rather, there is a global transition between roughly <240 K and >277 K (**Fig. 1d**, **Supp. Fig. 2**). This 240–277 K transition regime for M^{pro} does not coincide with the 180–220 K glass transition or dynamical transition threshold seen previously for other systems such as CypA [19], suggesting protein-to-protein variability. More locally in M^{pro}, as temperature increases, different regions experience distinct types of changes to conformational heterogeneity (**Fig. 5**), in line with previous multitemperature studies of other proteins [15]. These effects are not limited to surface-exposed side chains as one might naïvely expect, but rather encompass motions of buried side chains (**Fig. 6**), many backbone regions (**Fig. 4**, **Fig. 5**), and water molecules themselves (**Fig. 2**, **Fig. 3**). Our results here for M^{pro}, as well as a large body of previous literature for other systems, refute the assertion that X-ray crystallography under “unusual experimental conditions” like variable temperature is not useful for understanding proteins [23]. By contrast, our work is in line with computational analyses of B-factors suggesting that different alternative conformations for M^{pro} (and other systems) can be accessed by varying temperatures and/or the crystal lattice [31].

A key example of temperature-sensitive, protein-associated solvent is the mobile water H_2O_{int} that we observe in the M^{pro} active site (**Fig. 2**, **Fig. 3**). This rarely observed water’s intriguing placement, with multiple permitted positions along a swath between the catalytic dyad of His41 and Cys145, suggests it may play some role in the catalytic process [32]. Notably, recent structures of an acyl-enzyme intermediate structure (7KHP) and a C145A mutant product-bound structure (7JOY) of M^{pro} include a nearby water, ~1.5 Å away but aligned with our approximately collinear multitemperature H_2O_{int} swath

(**Fig. 3**), which the authors suggested may play a role as a deacylating nucleophile [32]. Questions about the functional role of H_2O_{int} could be explored in parallel with other experiments to probe details of the catalytic mechanism, such as variable pH to probe Cys145 oxidation and reactivity [18] and neutron crystallography to reveal a zwitterionic state of the catalytic dyad [33], although questions remain about the interpretation of such data [23].

Perhaps surprisingly, unlike temperature, high relative humidity during data collection does not affect H_2O_{int} in our structures (**Fig. 2**, **Fig. 3**). However, humidity does alter the solvation shell elsewhere nearby in the active site (**Fig. 2**, bottom right). This hints at the broader usefulness of humidity as an experimental variable in crystallography [34,35] for exploring solvent slaving to protein dynamics [36], solvent energetics in ligand binding [37], and other functionally relevant phenomena. Displaceable waters can also be exploited to design high-affinity small-molecule inhibitors, particularly when guided by water thermodynamics maps from simulations, as are available for M^{pro} and other SARS-CoV-2 proteins [38].

Phenix ensemble models [25] refined from our X-ray datasets helped us to illuminate temperature-dependent differences in conformational heterogeneity in certain areas of M^{pro} (**Fig. 4**, **Fig. 5**) that were concealed by more traditional model types [39]. Despite its utility in this and other work, there is significant potential for improvement of the ensemble refinement methodology through integration of more sophisticated molecular mechanics force fields like Amber [40] into the molecular dynamics component [25] to improve ensemble model geometry. Although it was beyond the scope of this study, ensemble models may reveal alternative conformational substates that are important for the catalytic cycle, which could be fruitfully targeted by small molecules for antiviral drug design.

Finally, our results emphasize the allure of allosteric inhibition of M^{pro} as an alternative therapeutic strategy. Our structures illustrate apparently coupled conformational motions that bridge the active site, substrate binding pocket, inter-domain interface, and parts of the broad dimer interface (**Fig. 5**, **Fig. 6**). This is particularly noteworthy since M^{pro} must dimerize to become an active enzyme [8,9]; inter-domain flexing has also been observed, even in crystals [23]. The intramolecular network we describe includes several sites that are distal from the active site and have already been characterized as ligandable by recent crystallographic screens of pre-existing drug molecules [11] and small-molecule fragments [12] (**Fig. 6**). Some new M^{pro} ligands have been shown by mass spectrometry to disrupt the M^{pro} dimer and allosterically inhibit catalysis, albeit weakly thus far [41], illustrating the potential of an allosteric strategy. As a complementary structure-based approach to current experiments on the dimeric crystal form of M^{pro}, future experiments could exploit mutations of the dimer interface to stabilize an inactive monomer, thus capturing a new structural target for crystallographic and solution screening for allosteric inhibitors that block dimerization. Ultimately, the present study offers insights into fundamental aspects of protein structural biophysics, and may also help pave the way for new efforts toward allosteric modulation of M^{pro} as a strategy for COVID-19 antiviral drug design.

Methods

Cloning, expression, and purification

Details of the cloning, expression, and purification will be reported elsewhere (Andi et al., manuscript under preparation). Briefly, the codon-optimized synthetic gene of full-length M^{pro} from SARS-CoV-2 was cloned into the pET29b vector. The cloned M^{pro} with C-terminal 6x histidine tag was expressed in *E. coli* using an auto-induction procedure [42]. Cells were harvested, lysed using bacterial protein extraction agents (B-PER, ThermoFisher Scientific) in the presence of lysozyme, and purified with

nickel-affinity chromatography followed by size exclusion chromatography. The histidine tag was cleaved by human rhinovirus (HRV) 3C protease (AcroBIOSYSTEMS) and further purified by reverse nickel-affinity chromatography. The purified protein was then dialysed overnight at 4°C against 30 mM HEPES pH 7.4, 200 mM NaCl, 1 mM TCEP; concentrated to ~7 mg/mL; and used for crystallization or stored at 80°C.

Crystallization

Plate-like crystals ranging from ~100–400 µm along the longest axis (~5–10 µm along the shortest axis) were grown via sitting drop vapor diffusion. After mixing a 1:1 ratio of ~7 mg/mL M^{pro} with a solution of 22% PEG 4000, 100 mM HEPES pH 7.0, 3–5% DMSO and incubating at a temperature of ~298 K, crystals were seen after 2–6 days. Crystals were harvested using 10 µm MicroMesh™ loops (MiTeGen), and enclosed in MicroRT™ capillaries (MiTeGen) for data collection at non-cryogenic temperatures.

X-ray data collection

X-ray data were collected at the National Synchrotron Light Source II (NSLS-II) beamline 17-ID-2 (FMX) [43] using an X-ray beam of energy 12.66 keV, corresponding to a wavelength of 0.9793 Å; a horizontal-bounce Si111 double crystal monochromator; and an Eiger X 16M pixel array detector (Dectris). Temperature at the sample goniometer was controlled using a Cryostream 800 (OxfordCryosystems). For the 298 K, 99.5% relative humidity dataset, RH was controlled with an HC-LAB Humidity Controller (Arinax). Ambient temperature was measured to be ~298 K, and ambient humidity was measured to be 36.7%. A new crystal was used for each dataset. Helical/vector data collection was used to traverse the length of each crystal, with a beam size of 10 x 10 µm. Local radiation damage did not appreciably accrue during the course of each single-crystal data collection, as indicated by $2F_o$-F_c electron density maps around carboxyl groups (data not shown).

X-ray data reduction and modeling

The data reduction pipeline fast_dp [44] was initially used for bulk data reduction during the beamtime, with selected data reprocessed using the xia2 DIALS [45] and xia2 3dii (XDS and XSCALE) pipelines [46], with xia2 3dii (XDS and XSCALE) also used for the generation of R_d statistics [47] (**Supp. Fig. 1**). Molecular replacement for each dataset was performed via Phaser-MR from the Phenix software suite, using PDB ID 6YB7 as a search model. Phenix AutoBuild [48] was used for initial model building and refinement, with subsequent iterative refinements performed using phenix.refine [49] and Coot [50]. After a few initial rounds of refinements, hydrogens were added using phenix.ready_set (Reduce [51] and eLBOW [52]). For refinement of each dataset, X-ray/stereochemistry weight and X-ray/ADP weight were refined and optimised. Geometric and protein statistics of the final models were evaluated via MolProbity [53,54] and the JCSG-QC check server (https://smb.slac.stanford.edu/jcsg/QC/). Data collection and refinement statistics are shown in **Table 1**.

Crystallographic ensemble models were generated using phenix.ensemble_refinement [25] in version 1.18.2-3874 of Phenix. Alternative conformations were first removed from the multiconformer models, and hydrogens were (re)added using phenix.ready_set. Next, a phenix.ensemble_refinement grid search was performed by repeating the simulation with four values of p_{TLS} (1.0, 0.9, 0.8, 0.6) and three values of wxray_coupled_tbath_offset (10, 5, 2.5), and using a random_seed value of 2679941. τ_x was set automatically according to the high-resolution limit of the dataset. From this grid, we present the analysis of the set of ensemble models that has both the lowest mean R_{free} and the lowest mean R_{free}-R_{work} gap: p_{TLS}=1.0, wxray_coupled_tbath_offset=2.5. Conclusions drawn for the set of ensemble models with lowest R_{free} per dataset, or the lowest R_{free}-R_{work} gap per dataset, were similar. Refinement statistics are shown in **Table 2**.

For F_o-F_o isomorphous difference map analysis, the phenix.fobs_minus_fobs_map executable in the Phenix software suite was used. Each elevated temperature was compared to 100 K. The 100 K multiconformer model was used for phasing for each difference map. For solvent content analysis, rwcontents v7.1.009 from the CCP4 suite [55] was used.

Data availability

Models and structure factors are available in the Protein Data Bank under the following PDB ID accession codes (see also **Table 1** and **Table 2**): 7MHF, 7MHG, 7MHH, 7MHI, 7MHJ, 7MHK for muticonformer models, and 7MHL, 7MHM, 7MHN, 7MHO, 7MHP, 7MHQ for ensemble models.

Acknowledgements

DAK is supported by NIH R35 GM133769.

This research was supported by the DOE Office of Science through the National Virtual Biotechnology Laboratory (NVBL) with funding from the Coronavirus CARES Act and additional funding was provided by Brookhaven National Laboratory (BNL) for research on COVID-19 (LDRD 20-042).

This research used beamline FMX (17-ID-2) of the National Synchrotron Light Source II, a U.S. Department of Energy (DOE) Office of Science User Facility operated for the DOE Office of Science by Brookhaven National Laboratory under Contract No. DE-SC0012704.

The Center for BioMolecular Structure (CBMS) is primarily supported by the National Institutes of Health, National Institute of General Medical Sciences (NIGMS) through a Center Core P30 Grant (P30GM133893), and by the DOE Office of Biological and Environmental Research (KP1605010).

Contributions

DAK conceived and supervised the project.
DAK, MRF, and SM planned the project.
AE, BTR, DK, BA, MRF, and DAK performed the experiments.
AE and BTR performed the data analysis.
AE, BTR, and DAK wrote the manuscript.
All authors contributed to manuscript editing.

Competing interests

The authors declare no competing interests.

ORCID

Ali Ebrahim*: 0000-0003-2661-381X
Blake T. Riley*: 0000-0003-2176-0503
Babak Andi: 0000-0002-7666-639X
Martin R. Fuchs: 0000-0001-9784-0927
Sean McSweeney: 0000-0002-3758-3161
Daniel A. Keedy: 0000-0002-9184-7586

References

1. Baum, A. *et al.* REGN-COV2 antibodies prevent and treat SARS-CoV-2 infection in rhesus macaques and hamsters. *Science* **370**, 1110–1115 (2020).
2. Beigel, J. H. *et al.* Remdesivir for the Treatment of Covid-19 - Final Report. *N. Engl. J. Med.* **383**, 1813–1826 (2020).
3. Boras, B. *et al.* Discovery of a Novel Inhibitor of Coronavirus 3CL Protease for the Potential Treatment of COVID-19. *bioRxiv* (2021) doi:10.1101/2020.09.12.293498.
4. V'kovski, P., Kratzel, A., Steiner, S., Stalder, H. & Thiel, V. Coronavirus biology and replication: implications for SARS-CoV-2. *Nat. Rev. Microbiol.* **19**, 155–170 (2021).
5. Berman, H. M. *et al.* The Protein Data Bank. *Nucleic Acids Res.* **28**, 235–242 (2000).
6. Jin, Z. *et al.* Structure of Mpro from SARS-CoV-2 and discovery of its inhibitors. *Nature* **582**, 289–293 (2020).
7. Zhang, L. *et al.* Crystal structure of SARS-CoV-2 main protease provides a basis for design of improved α-ketoamide inhibitors. *Science* **368**, 409–412 (2020).
8. Fan, K. *et al.* Biosynthesis, purification, and substrate specificity of severe acute respiratory syndrome coronavirus 3C-like proteinase. *J. Biol. Chem.* **279**, 1637–1642 (2004).
9. Goyal, B. & Goyal, D. Targeting the Dimerization of the Main Protease of Coronaviruses: A Potential Broad-Spectrum Therapeutic Strategy. *ACS Comb. Sci.* **22**, 297–305 (2020).
10. Vuong, W. *et al.* Feline coronavirus drug inhibits the main protease of SARS-CoV-2 and blocks virus replication. *Nat. Commun.* **11**, 4282 (2020).
11. Günther, S. *et al.* X-ray screening identifies active site and allosteric inhibitors of SARS-CoV-2 main protease. *Science* eabf7945 (2021).
12. Douangamath, A. *et al.* Crystallographic and electrophilic fragment screening of the SARS-CoV-2 main protease. *Nat. Commun.* **11**, 5047 (2020).
13. Chodera, J., Lee, A. A., London, N. & von Delft, F. Crowdsourcing drug discovery for pandemics. *Nat. Chem.* **12**, 581 (2020).
14. Fraser, J. S. *et al.* Accessing protein conformational ensembles using room-temperature X-ray crystallography. *Proc. Natl. Acad. Sci. U. S. A.* **108**, 16247–16252 (2011).
15. Keedy, D. A. *et al.* Crystal cryocooling distorts conformational heterogeneity in a model Michaelis complex of DHFR. *Structure* **22**, 899–910 (2014).
16. Kneller, D. W. *et al.* Structural plasticity of SARS-CoV-2 3CL Mpro active site cavity revealed by room temperature X-ray crystallography. *Nat. Commun.* **11**, 3202 (2020).
17. Kneller, D. W., Phillips, G., Kovalevsky, A. & Coates, L. Room-temperature neutron and X-ray data collection of 3CL Mpro from SARS-CoV-2. *Acta Crystallogr. Sect. F Struct. Biol. Cryst. Commun.* **76**, 483–487 (2020).
18. Kneller, D. W. *et al.* Room-temperature X-ray crystallography reveals the oxidation and reactivity of cysteine residues in SARS-CoV-2 3CL Mpro: insights into enzyme mechanism and drug design. *IUCrJ* **7**, (2020).
19. Keedy, D. A. *et al.* Mapping the conformational landscape of a dynamic enzyme by multitemperature and XFEL crystallography. *Elife* **4**, (2015).
20. Keedy, D. A. *et al.* An expanded allosteric network in PTP1B by multitemperature crystallography, fragment screening, and covalent tethering. *Elife* **7**, (2018).

21. Riley, B. T. *et al.* qFit 3: Protein and ligand multiconformer modeling for X-ray crystallographic and single-particle cryo-EM density maps. *Protein Sci.* **30**, 270–285 (2021).
22. Atakisi, H., Moreau, D. W. & Thorne, R. E. Effects of protein-crystal hydration and temperature on side-chain conformational heterogeneity in monoclinic lysozyme crystals. *Acta Crystallogr D Struct Biol* **74**, 264–278 (2018).
23. Jaskolski, M. *et al.* Crystallographic models of SARS-CoV-2 3CLpro: in-depth assessment of structure quality and validation. *IUCrJ* **8**, 238–256 (2021).
24. Halle, B. Biomolecular cryocrystallography: structural changes during flash-cooling. *Proc. Natl. Acad. Sci. U. S. A.* **101**, 4793–4798 (2004).
25. Burnley, B. T., Afonine, P. V., Adams, P. D. & Gros, P. Modelling dynamics in protein crystal structures by ensemble refinement. *Elife* **1**, e00311 (2012).
26. Woldeyes, R. A., Sivak, D. A. & Fraser, J. S. E pluribus unum, no more: from one crystal, many conformations. *Curr. Opin. Struct. Biol.* **28**, 56–62 (2014).
27. Fodor, J., Riley, B. T., Borg, N. A. & Buckle, A. M. Previously Hidden Dynamics at the TCR-Peptide-MHC Interface Revealed. *J. Immunol.* **200**, 4134–4145 (2018).
28. Broom, A. *et al.* Ensemble-based enzyme design can recapitulate the effects of laboratory directed evolution *in silico*. *Nat. Commun.* **11**, 4808 (2020).
29. Noske, G. D. *et al.* A Crystallographic Snapshot of SARS-CoV-2 Main Protease Maturation Process. *bioRxiv* (2021) doi:10.1101/2020.12.23.424149.
30. Bansia, H., Mahanta, P., Yennawar, N. H. & Ramakumar, S. Small Glycols Discover Cryptic Pockets on Proteins for Fragment-Based Approaches. *J. Chem. Inf. Model.* **61**, 1322–1333 (2021).
31. Pearce, N. M. & Gros, P. A method for intuitively extracting macromolecular dynamics from structural disorder. *bioRxiv* 2021.03.22.436387 (2021) doi:10.1101/2021.03.22.436387.
32. Lee, J. *et al.* Crystallographic structure of wild-type SARS-CoV-2 main protease acyl-enzyme intermediate with physiological C-terminal autoprocessing site. *Nat. Commun.* **11**, 5877 (2020).
33. Kneller, D. W. *et al.* Unusual zwitterionic catalytic site of SARS-CoV-2 main protease revealed by neutron crystallography. *J. Biol. Chem.* **295**, 17365–17373 (2020).
34. Kiefersauer, R. *et al.* A novel free-mounting system for protein crystals: transformation and improvement of diffraction power by accurately controlled humidity changes. *J. Appl. Crystallogr.* **33**, 1223–1230 (2000).
35. Sanchez-Weatherby, J. *et al.* Improving diffraction by humidity control: a novel device compatible with X-ray beamlines. *Acta Crystallogr. D Biol. Crystallogr.* **65**, 1237–1246 (2009).
36. Lewandowski, J. R., Halse, M. E., Blackledge, M. & Emsley, L. Protein dynamics. Direct observation of hierarchical protein dynamics. *Science* **348**, 578–581 (2015).
37. Darby, J. F. *et al.* Water Networks Can Determine the Affinity of Ligand Binding to Proteins. *J. Am. Chem. Soc.* **141**, 15818–15826 (2019).
38. Olson, B. *et al.* An online repository of solvation thermodynamic and structural maps of SARS-CoV-2 targets. *J. Comput. Aided Mol. Des.* **34**, 1219–1228 (2020).
39. Babcock, N. S., Keedy, D. A., Fraser, J. S. & Sivak, D. A. Model selection for biological crystallography. *bioRxiv* (2018).
40. Moriarty, N. W. *et al.* Improved chemistry restraints for crystallographic refinement by integrating the Amber force field into Phenix. *Acta Crystallogr D Struct Biol* **76**, 51–62 (2020).
41. El-Baba, T. J. *et al.* Allosteric Inhibition of the SARS-CoV-2 Main Protease: Insights from Mass Spectrometry Based Assays*. *Angew. Chem. Int. Ed Engl.* **59**, 23544–23548 (2020).

42. Studier, F. W. Protein production by auto-induction in high density shaking cultures. *Protein Expr. Purif.* **41**, 207–234 (2005).
43. Schneider, D. K. *et al.* FMX – the Frontier Microfocusing Macromolecular Crystallography Beamline at the National Synchrotron Light Source II. *J. Synchrotron Radiat.* **28**, 650–665 (2021).
44. Winter, G. & McAuley, K. E. Automated data collection for macromolecular crystallography. *Methods* **55**, 81–93 (2011).
45. Winter, G. *et al.* DIALS: implementation and evaluation of a new integration package. *Acta Crystallogr D Struct Biol* **74**, 85–97 (2018).
46. Kabsch, W. XDS. *Acta Crystallogr. D Biol. Crystallogr.* **66**, 125–132 (2010).
47. Diederichs, K. Some aspects of quantitative analysis and correction of radiation damage. *Acta Crystallogr. D Biol. Crystallogr.* **62**, 96–101 (2006).
48. Terwilliger, T. C. *et al.* Iterative model building, structure refinement and density modification with the PHENIX AutoBuild wizard. *Acta Crystallogr. D Biol. Crystallogr.* **64**, 61–69 (2008).
49. Afonine, P. V. *et al.* Towards automated crystallographic structure refinement with phenix.refine. *Acta Crystallogr. D Biol. Crystallogr.* **68**, 352–367 (2012).
50. Emsley, P. & Cowtan, K. Coot: model-building tools for molecular graphics. *Acta Crystallogr. D Biol. Crystallogr.* **60**, 2126–2132 (2004).
51. Word, J. M., Lovell, S. C., Richardson, J. S. & Richardson, D. C. Asparagine and glutamine: using hydrogen atom contacts in the choice of side-chain amide orientation. *J. Mol. Biol.* **285**, 1735–1747 (1999).
52. Moriarty, N. W., Grosse-Kunstleve, R. W. & Adams, P. D. electronic Ligand Builder and Optimization Workbench (eLBOW): a tool for ligand coordinate and restraint generation. *Acta Crystallogr. D Biol. Crystallogr.* **65**, 1074–1080 (2009).
53. Chen, V. B. *et al.* MolProbity: all-atom structure validation for macromolecular crystallography. *Acta Crystallogr. D Biol. Crystallogr.* **66**, 12–21 (2010).
54. Williams, C. J. *et al.* MolProbity: More and better reference data for improved all-atom structure validation. *Protein Sci.* **27**, 293–315 (2018).
55. Winn, M. D. *et al.* Overview of the *CCP*4 suite and current developments. *Acta Crystallogr. D Biol. Crystallogr.* **67**, 235–242 (2011).